Chapter 1
Magnetic Spectroscopy of Individual Atoms, Chains and Nanostructures

Jens Wiebe, Alexander A. Khajetoorians and Roland Wiesendanger

Abstract We review the magnetism of tailored bottom-up nanostructures which have been assembled of 3*d*-transition metal atoms on nonmagnetic metallic substrates. We introduce the newly developed methodology of single atom magnetometry which combines spin-resolved scanning tunneling spectroscopy (SPSTS) and inelastic STS (ISTS) pushed to the limit of an individual atom. We describe how it can be used to measure the magnetic moment, magnetic anisotropy, and g-factor of individual atoms, as well as their pair-wise Ruderman-Kittel-Kasuya-Yosida (RKKY)-interaction. Finally, we will show that, using these measured quantities in combination with STM-tip induced manipulation of the atoms, nanostructures ranging from antiferromagnetic chains and two-dimensional arrays over all-spin based logic gates to magnetic memories composed of only few atoms can be realized and their magnetic properties characterized.

1.1 Introduction

Magnetic nanostructures which are composed of atom-by-atom assembled arrays of atomic spins on nonmagnetic substrates have attracted a lot of attention in the last ten years as model systems to understand atomic-scale magnetism in the transition region between few interacting spins and macroscopic materials, as well as a platform for the proof of principle of nanospintronic technologies. The pathway into this field was paved by the ability of the scanning tunneling microscope (STM) tip to move individual atoms on a surface [1] and to measure the magnetic properties of single atoms [2, 3]. These advances enabled the study of the magnetic moment [3],

J. Wiebe · A. A. Khajetoorians · R. Wiesendanger (✉)
Department of Physics, University of Hamburg, Hamburg, Germany
e-mail: wiesendanger@physnet.uni-hamburg.de

J. Wiebe
e-mail: jwiebe@physnet.uni-hamburg.de

R. Wiesendanger (ed.), *Atomic- and Nanoscale Magnetism*, NanoScience and Technology, https://doi.org/10.1007/978-3-319-99558-8_1

g-factor [4–6], and magnetic anisotropy [4, 7–9] of individual atoms, the exchange interaction in pairs [10, 11], the properties of bottom-up chains [12–16] and two-dimensional arrays [14], as well as logic gates [17] and magnetic memories [18–20].

The magnetism of such nanostructures not only depends on the atom type used, but also crucially on the interaction of the atomic spin with the substrate conduction electrons which can dramatically modify the magnetic moment and the delocalization of the atomic spin. One strategy has been focused on the use of thin decoupling layers in order to strongly reduce the overlap of the electronic orbitals responsible for the atomic spin from the orbitals of the substrate conduction electrons [2, 7, 12, 15, 19], which typically enhances the "quantumness" of the nanostructures [20]. In this review, we will focus on the other extreme, i.e. in which the atomic spins are adsorbed directly onto a metallic substrate. As we will show, this enables to make use of a large range of substrate-conduction electron mediated Ruderman-Kittel-Kasuya-Yosida (RKKY)-interactions for the coupling between the atomic spins, which offers huge flexibility and tunability.

The review is organized as follows. Section 1.2 introduces the development of the experimental methodology towards characterizing the magnetic properties of single atoms on metallic surfaces. In Sect. 1.3 we review the application of these methods to atoms which are RKKY-coupled to magnetic layers. Furthermore, we consider the RKKY-coupling in pairs of atoms with a particular focus on the non-collinear contribution to the RKKY interaction. Section 1.4 deals with the investigation of tailored dilute chains and two-dimensional arrays of different numbers of atoms. Finally, we show the experimental realization of model systems of logic gates and magnetic memories made from only few atoms in Sect. 1.5.

1.2 Single Atom Magnetometry

For the investigation of the magnetic properties of individual atoms, two complementary scanning tunneling spectroscopy (STS) based techniques have been developed. The first is the spin-resolved STS (SPSTS) based measurement of the magnetization of an atom as a function of an externally applied magnetic field, which is introduced in Sects. 1.2.1 and 1.2.2. The second method is the inelastic STS (ISTS) based measurement of the excitations of the magnetization of an atom, which will be introduced in Sect. 1.2.3.

1.2.1 SPSTS on Individual Atoms

For the application of the technique of SPSTS to individual atoms, we first chose the sample system of cobalt atoms adsorbed on the (111) surface of platinum. This sample system had the following advantages: (i) it was extensively characterized by spatially averaging techniques, (ii) the magnetic moment of the Co atom is large

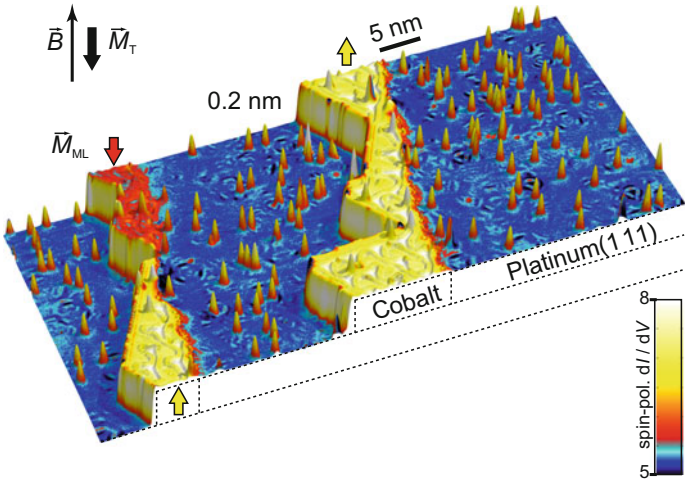

Fig. 1.1 Large-scale 3D rendering of a constant-current SP-STM image of single Co atoms and monolayer (ML) stripes on Pt(111), the first system utilized for the development of single atom magnetometry. The image was acquired with a chromium coated STM tip, magnetized antiparallel to the surface normal. An external magnetic field $\boldsymbol{B}$ can be applied perpendicular to the sample surface to change the magnetization of atoms $\boldsymbol{M}_{\mathrm{A}}$, ML stripes $\boldsymbol{M}_{\mathrm{ML}}$, or tip $\boldsymbol{M}_{\mathrm{T}}$. The ML appears red (yellow) when $\boldsymbol{M}_{\mathrm{ML}}$ is parallel (antiparallel) to $\boldsymbol{M}_{\mathrm{T}}$. Figure reprinted with permission from [3]. Copyright (2008) by AAAS

($m \approx 5\mu_{\mathrm{B}}$) and (iii) it has a large uniaxial magnetic anisotropy of $\mathcal{K} \approx -9\,\mathrm{meV}$ which forces the atomic spin of the Co to point perpendicular to the (111) surface (out-of-plane) [21].

Figure 1.1 shows an overview of the used sample. It consists of individual cobalt atoms on the (111) surface of platinum (blue) and cobalt monolayer (ML) stripes (red and yellow) which are attached to the step edges. The statistical distribution of the Co atoms on this surface results in a variety of different adsorption sites. Isolated Co atoms on Pt(111) can sit either on an fcc or on an hcp hollow site. Co atoms are adsorbed on the hcp or fcc areas of the Co ML. We also find closed-packed Co dimers, as well as pairs, triples or even larger ensembles with different inter-atomic distances (cf. Sect. 1.3.2). The advantage of the additional Co ML stripes is twofold. As will be shown in Sect. 1.3.1 it allows us to measure the magnetic interaction between the stripes and the individual Co atoms. Furthermore, the ML stripes which have a magnetization $\boldsymbol{M}_{\mathrm{ML}}$ perpendicular to the surface serve for the calibration of the orientation of the magnetization of the SPSTM tip. Using out-of-plane oriented (chromium coated) tips the up and down domains exhibit a different spin-resolved $\mathrm{d}I/\mathrm{d}V$ signal as visible in Fig. 1.1. Thereby, it is possible to characterize the spin polarization and magnetization $\boldsymbol{M}_{\mathrm{T}}$ of the foremost tip atom acting as a detector for the magnetization of the atom on the surface $\boldsymbol{M}_{\mathrm{A}}$, as will be described in the following.

In an SPSTS experiment, the spin-resolved differential tunneling conductance $\mathrm{d}I/\mathrm{d}V$ as a function of the applied sample bias voltage V, as long as V is not too

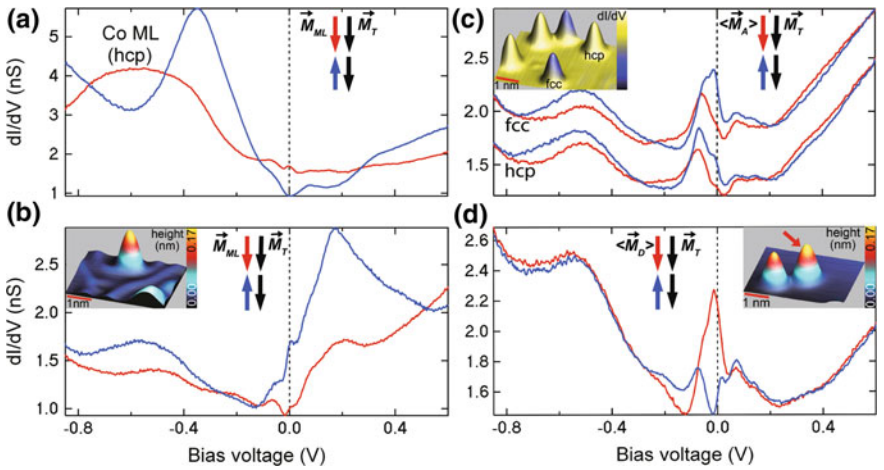

Fig. 1.2 SPSTS curves $\mathrm{d}I^{\uparrow\uparrow}/\mathrm{d}V(V)$ and $\mathrm{d}I^{\uparrow\downarrow}/\mathrm{d}V(V)$ for parallel (red) and antiparallel (blue) orientations of sample and tip magnetization, respectively, taken on **a** an hcp area of the Co ML, **b** a single atom on an fcc region of a ML (see inset), **c** single atoms sitting on fcc and hcp lattice sites on a Pt terrace (see inset), and **d** on the center of a dimer with both atoms sitting on nearest neighboring fcc sites on a Pt terrace (see inset). Figure reprinted with permission from [33]. Copyright (2010) by the American Physical Society

large, is given by

$$dI/dV(x, y, V) \propto \rho_T(E_\mathrm{F}) \cdot \rho_S(E_\mathrm{F} + \mathrm{eV}, \boldsymbol{R}_\mathrm{T}) \cdot (1 + P_\mathrm{T}(E_\mathrm{F}) \cdot P_\mathrm{S}(E_\mathrm{F} + \mathrm{eV}, \boldsymbol{R}_\mathrm{T}) \cos\theta)\,. \tag{1.1}$$

Here $\rho_S(E, \boldsymbol{R}_\mathrm{T})$ is the local electron density of states (LDOS) *above* the sample, $\rho_T(E_\mathrm{F})$ is the LDOS of the tip, P_S and P_T are their spin polarizations given by the difference between the majority and minority LDOSs normalized by their sum, i.e. $P = (\rho^\uparrow - \rho^\downarrow)/(\rho^\uparrow + \rho^\downarrow)$, $\boldsymbol{R}_\mathrm{T}$ is the position of the foremost tip atom and θ is the angle between its magnetization $\boldsymbol{M}_\mathrm{T}$ and that of the sample $\boldsymbol{M}_\mathrm{S}$. If the tip material has a much larger coercivity than the sample, as e.g. Cr, an appropriate external magnetic field $\boldsymbol{B}$ can align tip and sample magnetization parallel ($\uparrow\uparrow$) or antiparallel ($\uparrow\downarrow$). This results in the spin-resolved differential tunneling conductances $\mathrm{d}I^{\uparrow\uparrow}/\mathrm{d}V(V)$ and $\mathrm{d}I^{\uparrow\downarrow}/\mathrm{d}V(V)$. Thereby, the product of tip and sample spin-polarizations can be deduced from the measured magnetic asymmetry, assuming a constant distance between the tip and sample for the two cases ($\uparrow\uparrow$, $\uparrow\downarrow$), i.e.

$$\begin{aligned} A_\mathrm{mag}(V) &\equiv \left(\mathrm{d}I^{\uparrow\uparrow}/\mathrm{d}V - \mathrm{d}I^{\uparrow\downarrow}/\mathrm{d}V\right) / \left(\mathrm{d}I^{\uparrow\uparrow}/\mathrm{d}V + \mathrm{d}I^{\uparrow\downarrow}/\mathrm{d}V\right) \\ &= P_\mathrm{T}(E_\mathrm{F}) \cdot P_\mathrm{S}(E_\mathrm{F} + \mathrm{eV}, \boldsymbol{R}_\mathrm{T}). \end{aligned} \tag{1.2}$$

Thus, P_T has to be known in order to extract P_S.

Figure 1.2 illustrates how the sign of the spin-polarization of an atom was determined by measuring $\mathrm{d}I^{\uparrow\uparrow}/\mathrm{d}V(V)$ and $\mathrm{d}I^{\uparrow\downarrow}/\mathrm{d}V(V)$ on the Co ML which has a well-known $P_\mathrm{S}(E_\mathrm{F}+\mathrm{eV}, \boldsymbol{R}_\mathrm{T})$ [22]. Exactly the same tip was then used to characterize the Co atoms with unknown $P_\mathrm{S}(E_\mathrm{F}+\mathrm{eV}, \boldsymbol{R}_\mathrm{T})$ (Fig. 1.2b, c). As seen from Fig. 1.2a, the magnetic asymmetry A_mag defined in (1.2) is positive around E_F, i.e. $P_\mathrm{T}(E_\mathrm{F}) \cdot P_\mathrm{S}^\mathrm{ML}(E_\mathrm{F}, \boldsymbol{R}_\mathrm{T}) > 0$. On the other hand, first-principles calculations of the spin-resolved LDOS above the Co ML on Pt(111) yield $P_\mathrm{S}^\mathrm{ML}(E_\mathrm{F}, \boldsymbol{R}_\mathrm{T}) < 0$ [22]. Therefore, the tip must have a negative spin polarization at E_F, i.e. $P_\mathrm{T}(E_\mathrm{F}) < 0$. By comparison to the spectra measured with the same tip on a Co atom on the ML (Fig. 1.2b) and on a Co atom on the Pt substrate (Fig. 1.2c) we see that the strengths of the $\mathrm{d}I/\mathrm{d}V(V)$ signals at E_F for the parallel and antiparallel alignment of tip and sample (order of red and blue curves) is reversed with respect to the ML. This leads to the conclusion, that the sign of the vacuum spin polarization above the atoms around E_F is reversed with respect to that of the ML. Interestingly, this effect is already reversed back to the normal situation of the ML for a Co dimer, as visible in Fig. 1.2d.

1.2.2 Single-Atom Magnetization Curves

The magnetization of the atoms on Pt(111) in Fig. 1.2c was aligned parallel or antiparallel relative to the tip magnetization by changing the orientation of the external magnetic field $\boldsymbol{B}$. As a consequence, the intensity of the measured $\mathrm{d}I/\mathrm{d}V$ signal changes in a large energy interval around the Fermi energy. This signal change can be used to record the magnetization curves of single atoms as described in the following.

To this end, we use an anti-ferromagnetically coated tip, typically with Cr, whose magnetic moment orientation is not affected by $\boldsymbol{B}$. Then, $\mathrm{d}I/\mathrm{d}V$ at a particular voltage is measured as a function of $\boldsymbol{B}$ on the same atom at the same tip-sample distance (see Fig. 1.3a, b). The time resolution of SPSTS is typically much worse than the time scale of the magnetization switching of an atom which is adsorbed on a metal substrate. Therefore, $P_\mathrm{T}(E_\mathrm{F}) \cdot P_\mathrm{S}(E_\mathrm{F}+\mathrm{eV}, \boldsymbol{R}_\mathrm{T}) \cos\theta$ is proportional to the scalar product of the tip magnetization vector with the time average of the atom magnetization vector ($\langle \boldsymbol{M}_\mathrm{A} \rangle$), and the measured $\mathrm{d}I/\mathrm{d}V$ is given by (cf. 1.1)

$$\mathrm{d}I/\mathrm{d}V \propto (\mathrm{d}I/\mathrm{d}V)_0 + (\mathrm{d}I/\mathrm{d}V)_\mathrm{SP} \boldsymbol{M}_\mathrm{T} \cdot \langle \boldsymbol{M}_\mathrm{A} \rangle (\boldsymbol{B}) \ . \tag{1.3}$$

In words, recording of $\mathrm{d}I/\mathrm{d}V$ as a function of the external magnetic field results in the measurement of the projection of the time-average of the atom magnetization onto the tip magnetization direction.

In practice, a series of $\mathrm{d}I/\mathrm{d}V$ maps is recorded as a function of an external magnetic field $\boldsymbol{B}$ on an area with several atoms as shown in Fig. 1.3a, b. From this data set, the magnetization curve of each atom in this area is received by plotting the corresponding $\mathrm{d}I/\mathrm{d}V$ value averaged on top of each individual atom as a function of B. This is shown in Fig. 1.3c, d for several different atoms (on fcc and hcp stacking

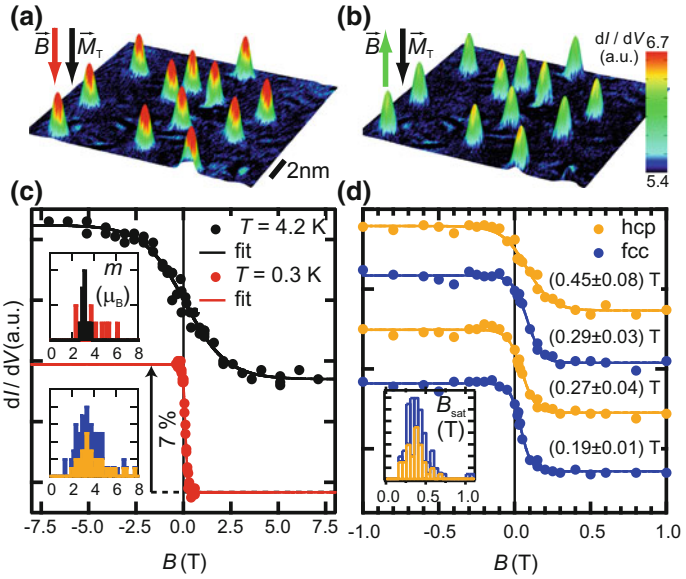

Fig. 1.3 **a**, **b** Spin-polarized dI/dV maps of 12 Co atoms on Pt(111) at $B = -0.5\,\mathrm{T}$ parallel to the tip magnetization $\boldsymbol{M}_\mathrm{T}$ (**a**) and $B = +0.5\,\mathrm{T}$ antiparallel to $\boldsymbol{M}_\mathrm{T}$ (**c**). The maps have been recorded using a Cr-coated tip that is magnetized perpendicular to the surface. **c** Magnetization curves from one of the atoms taken at different temperatures as indicated (dots). The solid lines are fits to the data (see text). The insets show the resulting histograms of the fitted magnetic moments (in μ_B) for 11 atoms at $T = 4.2\,\mathrm{K}$ (black) and at 0.3 K (red) (upper histogram), and for 38 hcp (orange) and 46 fcc (blue) atoms at 0.3 K (lower histogram, fcc bars stacked on hcp). **d** Magnetization curves of four atoms at 0.3 K with fit curves and resulting B_sat of 99% saturation. The inset shows the histogram of B_sat (in Tesla) for the same atoms used in the lower histogram in **c** (fcc bars stacked on hcp). Figure reprinted with permission from [3]. Copyright (2008) by AAAS

position) and at two different temperatures $T = 4\,\mathrm{K}$ and $T = 0.3\,\mathrm{K}$. The resulting s-shaped curves resemble the magnetization curves of paramagnetic atoms.

Such single-atom magnetization curves can be used to determine the magnetic moment of the particular atom, as shown in Fig. 1.3c, d. For this purpose, the curves were fitted to the following classical model:

$$E(\theta, B) = -mB\cos\theta + \mathcal{K}(\cos\theta)^2 \tag{1.4}$$

$$\langle M_\mathrm{A}\rangle \propto \frac{\int d\theta \sin\theta e^{\frac{-E(\theta,B)}{k_\mathrm{B}T}}}{\int d\theta e^{\frac{-E(\theta,B)}{k_\mathrm{B}T}}} \tag{1.5}$$

Here, m is the effective magnetic moment of the atom, and $\mathcal{K}$ is its uniaxial magnetic anisotropy energy in the direction of $\boldsymbol{B}$. Please note that usually, m and $\mathcal{K}$ can only be determined independently from magnetization curves in two perpendicular magnetic field directions. Here, we considered the $\mathcal{K}$-value known from XMCD measurements [21]. The fitted curves which are shown in Fig. 1.3c, d on top of the

Table 1.1 Values of magnetic moments m determined from single atom magnetization curves for different sample systems [3, 5]. The given errors are reflecting the variation from the fitting of the magnetization curves of different atoms on the surface

System	m in μ_B
fcc Co on Pt(111)	3.5 ± 1.5
hcp Co on Pt(111)	3.9 ± 1.5
Fe on Cu(111)	3.5 ± 1.5

measured curves nicely reproduce the data. The resulting magnetic moments are given in the insets of Fig. 1.3c.

A similar measurement and analysis has been done for Fe atoms on Cu(111) and the determined magnetic moments are summarized in Table 1.1. While the values for Co on Pt(111) are considerably smaller than the ones which have been determined by XMCD measurements [21], the values for Fe on Cu(111) fit with values from XMCD [23].

Most importantly, even though the atom has a strong magnetic anisotropy, its magnetization is not stable but switches on a time scale which is much faster than the detection limit of conventional SPSTM. However, we will see in Sect. 1.5 that direct exchange coupling of only three Fe atoms already increases the lifetime of the magnetization to hours. Moreover, there is a strong scattering of m which is a result of the residual RKKY interaction from the background of statistically distributed atoms. We will later see, how the single-atom magnetization curves can be used in order to measure this RKKY interaction in pairs of atoms as a function of their distance (see Sect. 1.3.2).

1.2.3 Magnetic Field Dependent Inelastic STS

A complementary STS based method for the detection of the spin excitations of single atoms is inelastic STS (ISTS). The method was originally applied to magnetic atoms whose spin is decoupled from the conduction electrons of a metal substrate by using thin decoupling layers [2]. Later it was also adapted to the investigation of magnetic atoms adsorbed directly on the surface of a metal [4–6, 8]. The method is illustrated in Fig. 1.4a for an fcc Fe atom on Pt(111). It is based on magnetic field dependent ISTS which reveals steps at positive and negative bias voltages V (symmetrically around zero bias) shifting as a function of B. The steps are located at the energies $E_{ex} = |\pm eV|$ of the spin excitations of the atom (in this case only one). Typically, effective spin Hamiltonians of the form $\hat{\mathcal{H}} = K \cdot \hat{S}_z^2 - g\mu_B \hat{\boldsymbol{S}} \cdot \boldsymbol{B}$ have been considered for the analysis of such ISTS data. Within this model, the zero field E_{ex} reflects the magnetic anisotropy parameter K of the atomic spin via $K = E_{ex}/(2S-1)$. E_{ex} is shifting with B due to the Zeeman splitting and the corresponding slope is directly proportional to the g-factor of the atom.

For a transition metal atom which is adsorbed directly on a metal substrate, there are typically strong charge fluctuations within the d-orbitals, such that the spin quan-

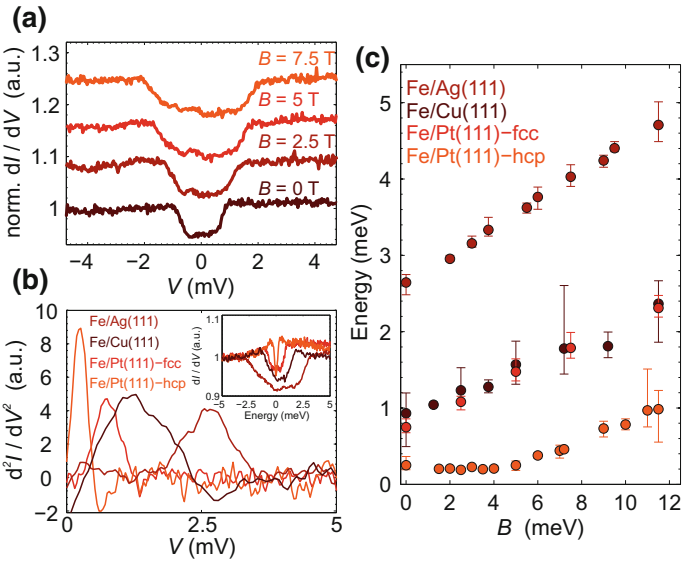

Fig. 1.4 **a** ISTS taken at various out-of-plane magnetic fields, as indicated, on an fcc Fe atom adsorbed on Pt(111) [4]. **b** ISTS taken at zero magnetic field for Fe atoms on various substrates as indicated (second derivative, the corresponding differential conductance data is given in the inset). **c** Spin-excitation energy extracted from the magnetic field dependent ISTS of the various systems as indicated. The data has been taken from [4–6]

Table 1.2 Values of magnetic anisotropy parameter K from the effective spin model and g-factor of Fe on three different substrates determined from magnetic field dependent ISTS [4–6]. The indicated spin quantum numbers S are estimated via $m = g\mu_B S$ from the magnetic moment m measured by single-atom magnetization curves for Cu(111) [5] or calculated from DFT for Pt(111) [4] and Ag(111) (here the calculated spin moment is 3.5 μ_B)

System	S	K in meV	g
hcp Fe on Pt(111)	5/2	0.08	2
fcc Fe on Pt(111)	5/2	−0.19	2.4
Fe on Cu(111)	3/2	−0.5	2.1
Fe on Ag(111)	1	−2.7	3.13

tum number S is no longer well-defined [5, 24]. Surprisingly, even in this case, the excitations can be reasonably reproduced by the effective spin model assuming the magnetic anisotropy and an exchange mechanism for the spin-flip probability, by using an S closest to the magnetic moment of the atom [24]. The latter can be either extracted experimentally from single-atom magnetization curves (Sect. 1.2.2) or determined from DFT calculations.

Figure 1.4b, c illustrate a comparison of magnetic-field dependent ISTS taken on Fe atoms adsorbed on three different substrates. The extracted parameters are shown in Table 1.2. Obviously both, K and g, vary for the different systems, and K even

changes from out-of-plane to easy-plane magnetic anisotropy from fcc to hcp for Fe on Pt(111) (see the sign change). Thus, K and g crucially depend on the interaction of the Fe atom with the substrate. Single-atom magnetization curves and ISTS not only were used to reveal the magnetic moment of individual atoms, but also to study their magnetic interactions as will be shown in the following.

1.3 Measurement of the RKKY Interaction

1.3.1 RKKY Interaction Between a Magnetic Layer and an Atom

Figure 1.5a–c illustrate out-of-plane magnetization curves that have been recorded on one of the Co monolayer stripes of the sample of Fig. 1.1 and on three Co atoms with different separations to the stripe. As visible from the square shaped hysteresis, the coercive field of the monolayer stripe is 0.5 T. In stark contrast to the s-shaped magnetization curves of the uncoupled Co atoms (see Fig. 1.3), the curves measured on the three atoms close to the monolayer show hysteresis. This effect can be traced back to the RKKY interaction between the atom and the monolayer. The corresponding exchange bias fields B_{ex} (see arrows in Fig. 1.5a–c) which are given by the magnetic fields at which the RKKY interaction energy J is compensated by the Zeeman energy of the atom can be used to extract the absolute value of J via $|J| = m B_{\mathrm{ex}}$ using the magnetic moment of the Co atom of $m \approx 3.7 \mu_B$. On the other hand, the sign of J is given by the symmetry of the magnetization curve in Fig. 1.5 [3, 32]. The extracted values are plotted in Fig. 1.5d as a function of distance d of the atom from the monolayer stripe. It shows the typical oscillatory damped behavior of the RKKY interaction. Fits to isotropic models of the asymptotic RKKY interaction $J(d) = J_0 \cdot \cos(2k_F d)/(2k_F d)^D$ with the Fermi wavevector k_F and different assumed dimensionalities D are shown in Fig. 1.5d. D is determined by the dimensionality of the electron system that induces the interaction, which is not known a priori, since it depends on the localization character of the underlying substrate-electron states that induce the interaction. The best fit is found for $D = 1$ which leads to the conclusion that the responsible substrate-electron states are strongly localized in the surface and have a Fermi wavelength of $\lambda_F = 2$–3 nm.

1.3.2 RKKY Interaction Between two Atoms

The RKKY interaction also leads to a measurable coupling between single Co atoms as illustrated in Fig. 1.6. The figure shows single-atom magnetization curves, that have been measured on the two atoms of Co pairs with decreasing separations between 2 and 5 lattice constants. Again, the magnetization curves show clear deviations from the s-shaped magnetization curves of the uncoupled Co atoms (see

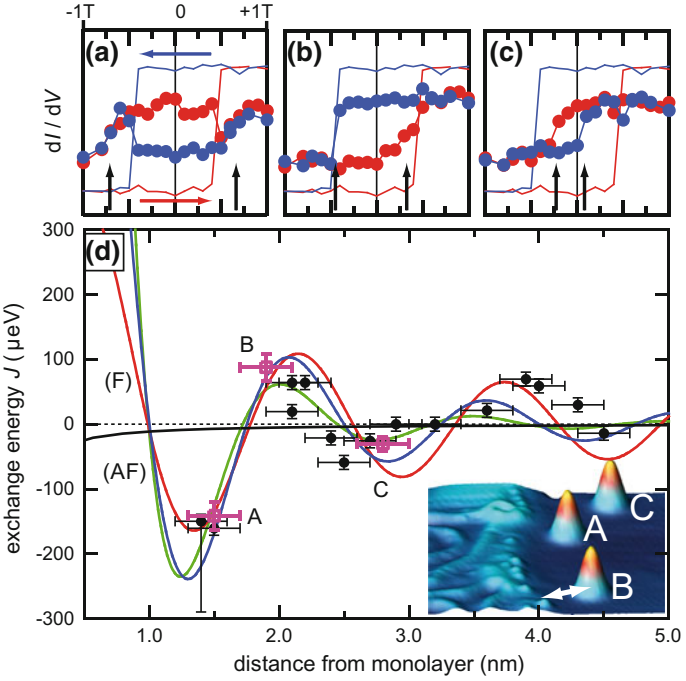

Fig. 1.5 **a**, **b**, **c** Out-of-plane magnetization curves measured on the monolayer (straight lines) and on three atoms (dots) A, B and C with different distances from the monolayer (see inset in (**d**), blue (red) color indicates down (up) sweep). The vertical arrows indicate the magnetic field B_{ex} at which the RKKY interaction between the Co atom and monolayer is compensated by the Zeeman energy. **d** Dots: Extracted RKKY exchange energy as a function of distance between atom and monolayer. The black line is the dipolar interaction. The red, blue and green lines are fits assuming 1D, 2D and 3D itinerant electron systems. Figure reprinted with permission from [3]. Copyright (2008) by AAAS

Fig. 1.3). While for some pairs, the two magnetization curves are still s-shaped, but with a steeper slope around zero magnetic field (Fig. 1.6f, k), other pairs reveal an additional oscillation or a plateau around zero magnetic field (Fig. 1.6g–j). While the former indicates ferromagnetic coupling, the latter is a result of an antiferromagnetic interaction between the two atoms. Note, that there is no hysteresis, indicating that the atoms are coupled, but still fluctuate on a time scale much faster than our measurement. This conclusion is substantiated and quantitatively analysed within the following Ising model:

$$\mathcal{H} = -\frac{1}{2} \sum_{i,j(i\neq j)} J_{ij}\left(\boldsymbol{r}_{ij}\right) \boldsymbol{S}_i \cdot \boldsymbol{S}_j - \sum_i m_i \boldsymbol{S}_i \cdot \boldsymbol{B} \tag{1.6}$$

where $i(j)$ labels the atoms 1 and 2 in the pair, $\boldsymbol{S}_i = \pm \boldsymbol{e}_z$ with the unit vector $\boldsymbol{e}_z$ along the surface normal z, and the absolute values of the magnetic moments m_i

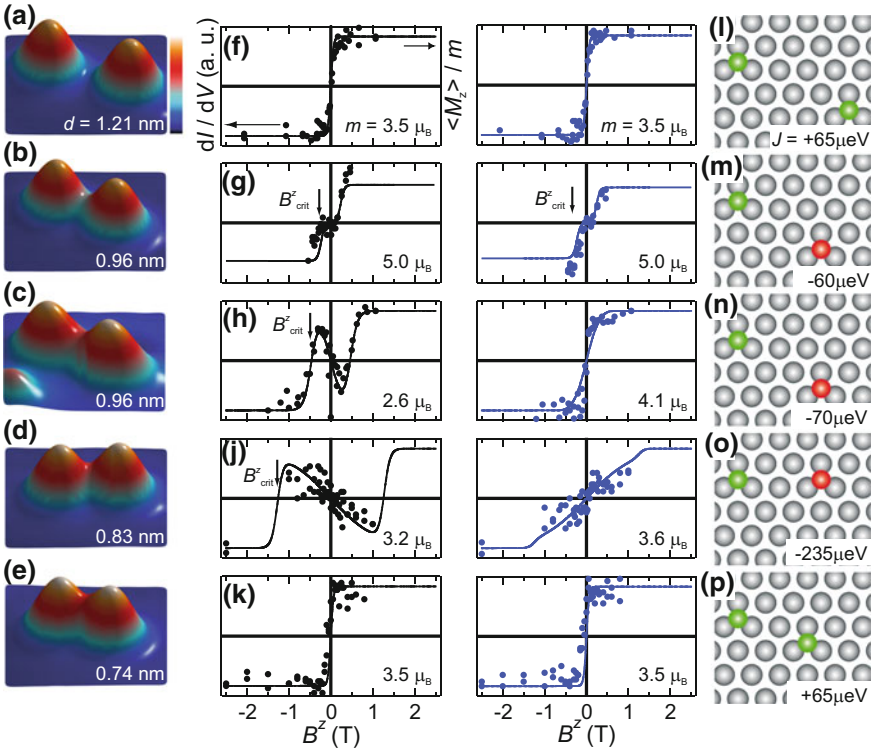

Fig. 1.6 Out-of-plane single-atom magnetization curves of Co pairs on Pt(111) with different distances shown in the STM images in **a**–**e**, and corresponding ball models of the positions of the two atoms in the pair on the substrate lattice in **l**–**p**. **f**–**k** shows the single-atom magnetization curves measured on the left atom (black dots) and on the right atom (blue dots) of each pair. The straight lines are calculated from the Ising model assuming magnetic moments m given in each curve and RKKY interaction energies given in **l**–**p**. Figure reprinted with permission from [11]. Copyright (2010) by Springer Nature

(in μ_B). While the first term describes the distance dependent exchange interaction, the second term is the Zeeman energy. Note that the Ising limit is justified by the large out-of-plane magnetic anisotropy of $\mathcal{K} = -9.3$ meV of the system of Co atoms on Pt(111) [21]. The results of the fits of the model to the measured single atom magnetization curves by variation of m_1, m_2 and J_{12} are shown in Fig. 1.6f–k as straight lines. They demonstrate an excellent reproduction of the measured data. The corresponding values of the RKKY interaction energy for about 10 pairs with different distances d placed at different locations on the bare Pt(111) substrate are shown in Fig. 1.7a. It reveals the typical oscillation between ferromagnetic ($J > 0$) and antiferromagnetic ($J < 0$) interaction which is reminiscent of the RKKY interaction.

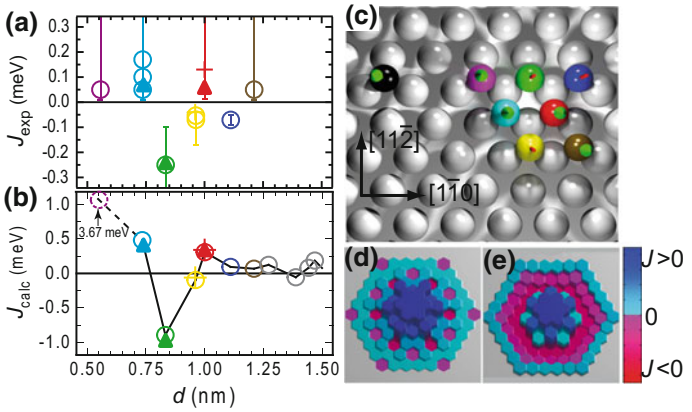

Fig. 1.7 **a** Measured RKKY interaction energy J_{exp} extracted from the single-atom magnetization curves of Co pairs on Pt(111) as a function of the distance d of the two atoms in the pair. **b** shows the corresponding values J_{calc} from the first-principles calculation. The data points are colored corresponding to the lattice positions of the atoms in the pairs shown in **c** where the first atom stays on the position of the black sphere. **d** Map of the calculated J's in the (111) plane where each hexagon corresponds to the lattice site of the second atom in a specific pair with the first atom fixed in the center. **e** Same as **d**, but with J's from the 2D isotropic RKKY model evaluated on the discrete lattice. Figure reprinted with permission from [11]. Copyright (2010) by Springer Nature

The experimental data of J was compared to ab initio calculated values from density functional theory utilizing the KKR method [11] (Fig. 1.6b). While the qualitative behavior of the experimental data is nicely reproduced by the calculation, the calculated values are a factor of about three times larger than the experimental ones. Most interestingly, the RKKY interaction shows a strong directionality, which is revealed by a 3D plot of the calculated J's in Fig. 1.7d in comparison to a similar plot of a 2D isotropic RKKY model given in Fig. 1.7e.

1.3.3 Dzyaloshinskii–Moriya Contribution to the RKKY Interaction

As shown in the preceding section, single-atom magnetization curves of the out-of-plane magnetization of interacting Co atoms on Pt(111) are approximately described within the Ising limit due to their large uniaxial out-of-plane anisotropy. We therefore so far only considered the usual Heisenberg contribution J to the RKKY interaction. However, as theoretically shown by Smith [25] and Fert [26] there is an additional Dzyaloshinskii–Moriya (DM) contribution to the RKKY interaction if the interaction is mediated by a heavy-element substrate featuring strong spin-orbit coupling. The magnetization of the coupled pair of quantum spins with spin operators $\hat{\boldsymbol{S}}_1$ and $\hat{\boldsymbol{S}}_2$ can then be quantified by the following spin Hamiltonian:

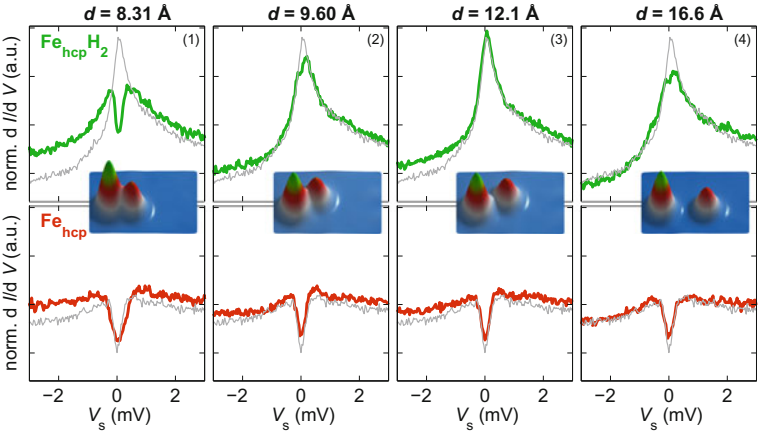

Fig. 1.8 ISTS of $Fe_{hcp}H_2$ (green) and Fe_{hcp} (red) within selected pairs of different distance as shown in the topographs in the insets. In comparison, the spectra measured on the corresponding isolated atoms are shown in gray. Figure reprinted with permission from [27]. Copyright (2016) by Springer Nature

$$\hat{\mathcal{H}} = -J_{12}\left(\hat{\boldsymbol{S}}_1 \cdot \hat{\boldsymbol{S}}_2\right) - \boldsymbol{D}_{12} \cdot \hat{\boldsymbol{S}}_1 \times \hat{\boldsymbol{S}}_2 + \sum_i K_i \left(\hat{S}_i^z\right)^2 - \sum_i g_i \mu_B \hat{\boldsymbol{S}}_i \cdot \boldsymbol{B} \qquad (1.7)$$

where g_i are the g-factors of the two atoms. In comparison to (1.7) the additional term with the so called DM-vector $\boldsymbol{D} = \left(D_{||}, D_{\perp}, D_z\right)$ (see the definition of the components in Fig. 1.9d) favors a perpendicular orientation of the two spins.

In order to investigate the non-collinear behavior of the RKKY interaction, we studied pairs of Fe atoms and Fe-hydrogen complexes on Pt(111). Unlike Co atoms, the Fe atoms and complexes can exhibit very small values of magnetic anisotropy, both in-plane and out-of-plane, and Kondo behavior. Atoms with weak easy-plane magnetic anisotropy are no longer correctly described by Ising-like spins and non-collinear interactions need to be considered [24]. By investigating pairs of an Fe-hydrogen complex and an Fe atom on Pt(111) using the method of magnetic-field dependent ISTS in comparison to simulations within a Kondo model based on (1.7) [27], we were indeed able to reveal the DM contribution to the RKKY interaction. Figure 1.8 shows ISTS curves of the two atoms in such pairs of increasing distances. The Fe atom Fe_{hcp} adsorbed on the hcp lattice site has the usual spin-excitation (cf. Fig. 1.4b). The Fe-hydrogen complex $Fe_{hcp}H_2$ consisting of two H atoms and an Fe_{hcp} atom reveals a resonance at zero bias voltage (see the gray curve of the isolated $Fe_{hcp}H_2$) which is due to a multi-orbital Kondo effect. When these two adsorbates are coupled, the interplay of J and $\boldsymbol{D}$ induces a splitting of the Kondo resonance of $Fe_{hcp}H_2$ and a modification of the magnetic excitation of Fe_{hcp} as compared with the isolated atoms, which is oscillating as a function of distance. By

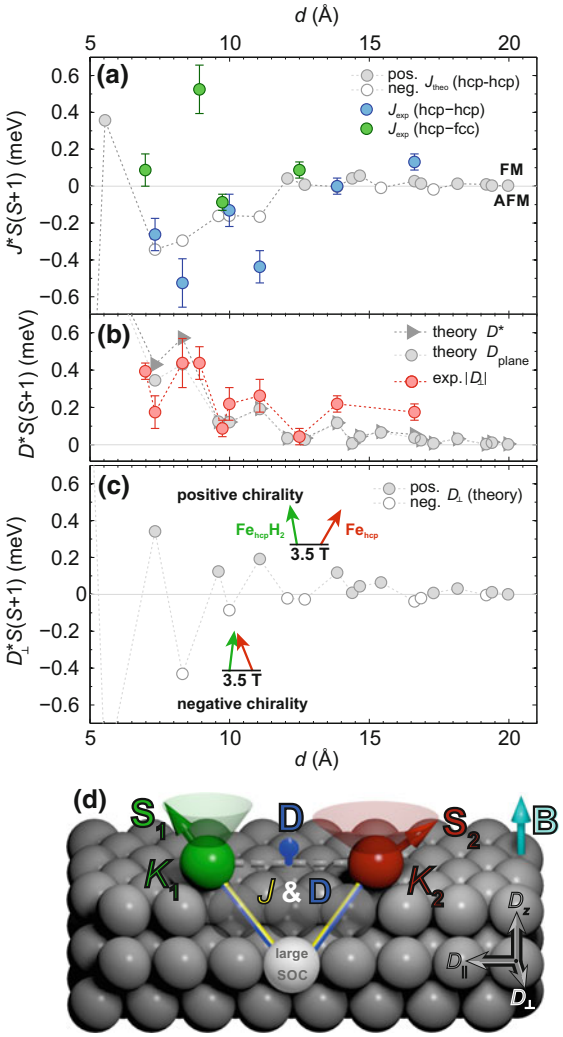

Fig. 1.9 **a**, **b** Experimentally determined values of the Heisenberg (J) and the DM interaction (D, colored circles) between two Fe impurities on Pt(111) compared with the theoretical ab initio calculation of J and the different components of the DM vector (gray and white circles and triangles). **c** Calculated perpendicular component of the DM vector resulting in a different rotational sense of the magnetizations of the two impurities for positive and negative sign as indicated by the arrows. **d** Cartoon diagram of the J and DM contributions to indirect conduction electron-mediated exchange interactions between two magnetic atoms with spins S_1 and S_2, and magnetic anisotropies K_1 and K_2. The interaction is mediated by scattering of conduction electrons at a substrate atom (gray) with strong spin-orbit coupling (SOC). The arrows show the orientation of the experimental magnetic field B and components of the DM vector [27]

fitting according magnetic field dependent spectra with simulations, we were able to extract both, J and the largest component of the DM-vector $D_\perp$, as a function of separation d of the two magnetic impurities (Fig. 1.9a, b). For most of the distances, the experimentally determined values are nicely reproduced by a theoretical ab initio calculation. Most interestingly, the resulting oscillatory behavior of the sign of $D_\perp$ with increasing distance shown in Fig. 1.9c induces a distance dependent chirality of the non-collinear magnetization in the pair as shown in the inset of Fig. 1.9c. The same interaction, which is determined here for pairs of atoms, is also responsible for the formation of complex non-collinear magnetization states as skyrmions in layers of magnetic materials.

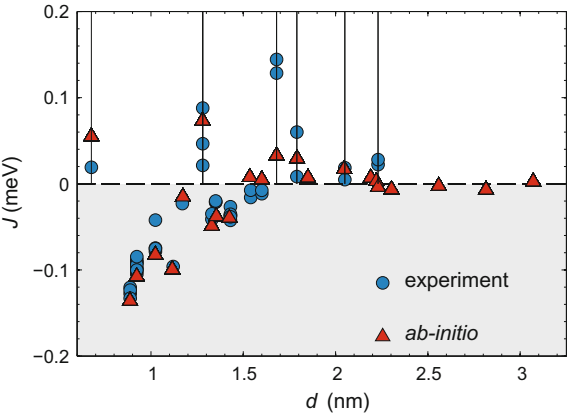

Fig. 1.10 Distance dependency of the RKKY interaction in pairs of Fe atoms on Cu(111). Measured (blue circles) and KKR-calculated (red triangles, renormalized by a factor of 1/2) exchange energy J_{ij} in pairs of Fe atoms on Cu(111) as a function of separation. Data taken from [14]

1.4 Dilute Magnetic Chains and Arrays

In Sect. 1.3, it has been shown how the experimental techniques SPSTS and ISTS can be used to measure maps of the distance dependent RKKY interaction in pairs of atoms adsorbed to metallic substrates. Using such maps it is possible to design artificial nanostructures of a larger number of atoms with tailored interatomic couplings and different topology, e.g. chains or two-dimensional arrays, which can then be built via STM-tip induced atom manipulation. Afterwards, the magnetization curve of each atom within such arrays can be measured by SPSTS and compared to simulations. This methodology has been applied to the system of Fe atoms on Cu(111) as will be shown in the following.

Due to the relatively small spin-orbit interaction of Cu as compared to Pt [28], and the large uniaxial out-of-plane magnetic anisotropy of Fe on Cu(111) of $K = -0.5$ meV the DM contribution to the RKKY interaction can be neglected in this case [29]. The measured distance dependence of the Heisenberg part J of the RKKY interaction is shown in Fig. 1.10. Note, that there is a pronounced minimum at a distance of $d \approx 1$ nm, where the RKKY interaction is antiferromagnetic with a large strength of $J \approx -0.1$ meV.

Dilute magnetic nanostructures of different topology and number of atoms (chains, 2D arrays) with nearest neighbor distances in the range of this minimum of strongest antiferromagnetic coupling have been assembled using STM-tip induced manipulation as displayed in Fig. 1.11a. Indeed, in the spin-resolved STM image taken in a small magnetic field of $B \approx -0.7$ T they typically show a spin-contrast alternating between dark and bright revealing the trend of an antiferromagnetic alignment of neighboring atoms. The detailed investigation of the underlying magnetization states of all nanostructures is described in [14]. As an example, Fig. 1.11b–m show the investigation of the Fe chains of six and seven atoms, and of a Kagomé of 12 Fe atoms.

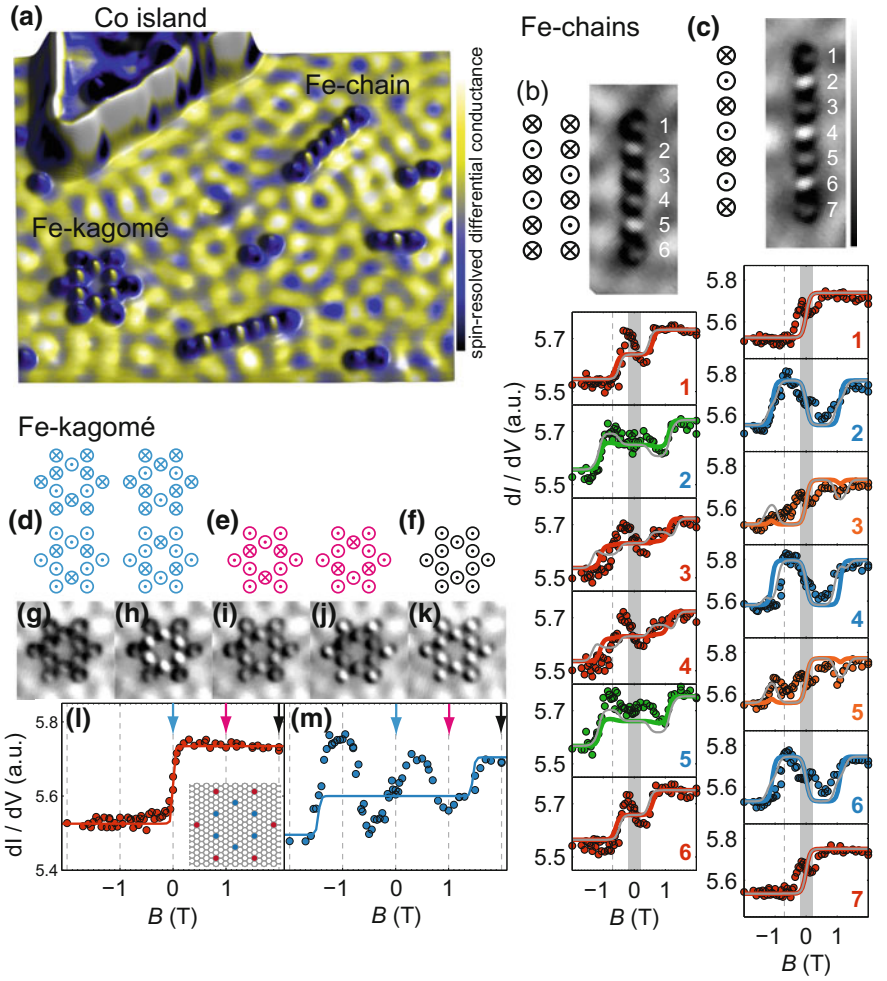

Fig. 1.11 **a** SPSTS image taken at $B \approx -0.7$ T of different manipulated magnetic arrays consisting of RKKY coupled Fe atoms with a neighbor distance of $d \approx 1$ nm on Cu(111) (hillocks). **b**, **c** Top panels: magnetization states from the Ising model (left, partly degenerate) and SPSTS images (right) of chains of anti-ferromagnetically coupled Fe atoms with a length of six (**b**) and seven (**c**) atoms. Bottom panels: magnetization curves measured (circles) on each atom of the chains. The magnetic images have been taken at B indicated by the dashed vertical line. **d–f** degenerate magnetization states of an Ising model for an array of 12 anti-ferromagnetically coupled atoms forming a Kagomé at B as indicated by the arrows in **(l, m)**. **g–k**, SPSTS images of the Kagomé recorded at B as indicated by the dashed lines in **(l, m)**. **l**, **m** magnetization curves measured on the Kagomé atoms (circles). Thick colored and thin gray lines in the magnetization plots show magnetization curves as calculated from different Ising models (see text). The gray shaded areas show the B range, where the experimental magnetization curve deviates from the Ising model. Images partly taken from [14]

The single-atom magnetization curves taken on each atom of the six (Fig. 1.11b) and seven (Fig. 1.11c) atom chains reveal striking differences between the even and odd number chains. For the odd number chain, the magnetization of nearest neighbors alternates between up and down in a magnetic field of $B \approx \pm 0.5\,\mathrm{T}$ indicating the stabilization of an antiferromagnetic Néel state (top part of Fig. 1.11c). In contrast, for the even number chain (Fig. 1.11b), this is not the case for all neighbors (see atom 3 and 4). As shown by simulations within the Ising model (1.7) using the RKKY couplings from the pairs (Fig. 1.10), this can be ascribed to the superposition of multiple degenerate magnetization states for the even number chains (top part of Fig. 1.11b). Interestingly, for the best possible simulation of the magnetization curves within the Ising model, the next-nearest neighbor interaction is crucial. This is shown by a comparison of the simulated curves using the same nearest neighbor J but different next-nearest neighbor interactions with the experimental data (see colored and gray lines in Fig. 1.11b, c). The best agreement was found (gray curves) when the next-nearest neighbor J's from an ab initio calculation of the full chain were used [14].

The investigation of the Kagomé using SPSTS revealed a superposition of four degenerate magnetization states in zero magnetic field (Fig. 1.11d, i). This degeneration is first partly lifted in a small magnetic field where only two degenerate states are remaining (Fig. 1.11e, h, j), and finally all atoms are aligned in a strong magnetic field (Fig. 1.11f, g, k). Surprisingly, there is a strong discrepancy between the measured and calculated magnetization curves for the inner six atoms of the Kagomé in a large magnetic field range between $B = \pm 1.5\,\mathrm{T}$ (Fig. 1.11m). Similarly, there are deviations for some atoms in the chains in a small field window around zero magnetic field (see gray shaded areas). These discrepancies are either due to hidden magnetic moments [14] or effects of a rather slow magnetization dynamics of the arrays.

1.5 Logic Gates and Magnetic Memories

Model systems of magnetic memories and logic gates can be realized using STM-tip induced atom manipulation of the investigated systems of atoms and their interactions.

As shown in the preceding section Sect. 1.4, the antiferromagnetic state of an RKKY coupled chain can be stabilized using a small magnetic field. Moreover, it was shown in Sect. 1.3.1 that the magnetization of an individual atom can be stabilized by RKKY interaction to patches of ferromagnetic monolayers. It is therefore an obvious question to ask, whether the antiferromagnetic state of an RKKY coupled chain could as well be stabilized by RKKY coupling to a ferromagnetic island. Such a stabilization would enable device concepts as illustrated in Fig. 1.12a. Here, the ends of two chains of anti-ferromagnetically coupled atoms are each strongly coupled to a ferromagnetic island (input islands 1 and 2). The chains are intended to transfer the information of the magnetization state of the two input islands towards the actual gate region. The latter consists of the other two end atoms of the two chains (input

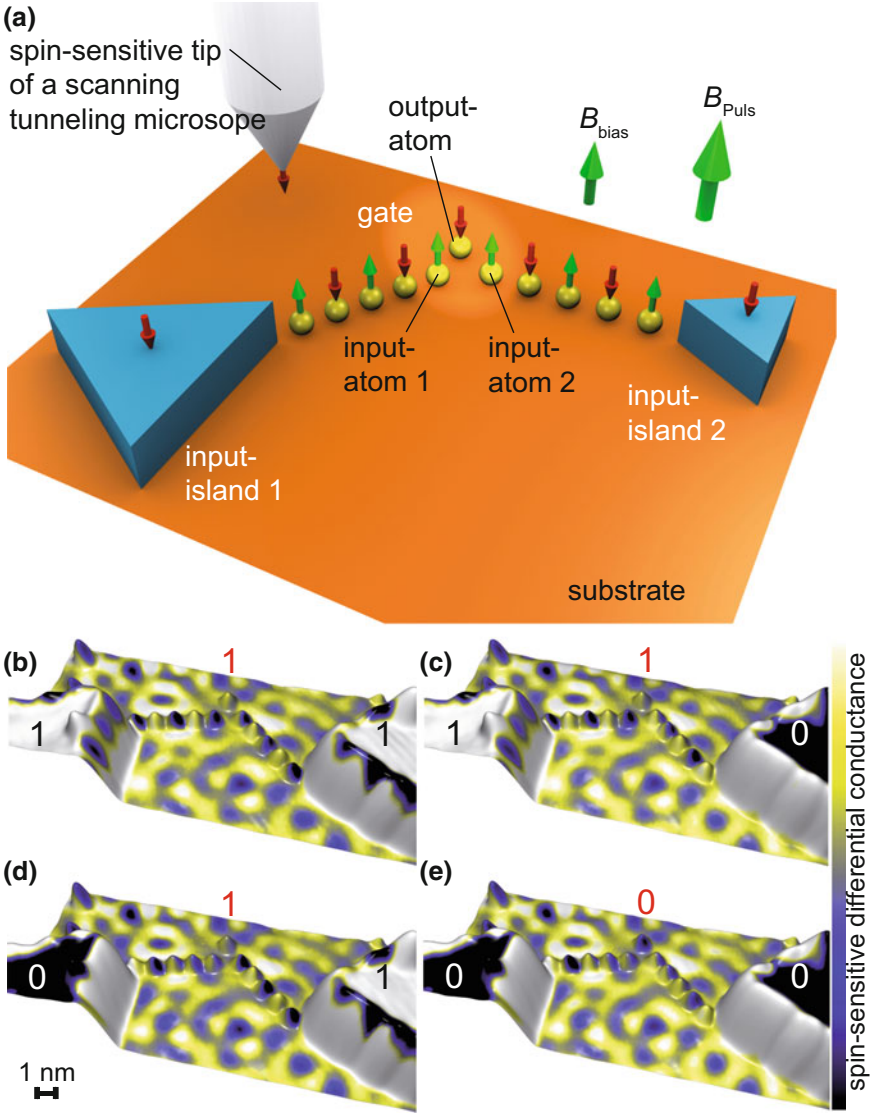

Fig. 1.12 **a** Concept of a logic gate made of two chains of anti-ferromagnetically RKKY coupled magnetic atoms (yellow spheres), which are exchange-coupled to two "input islands" (1, 2) of different size, consisting of patches of ferromagnetic layers. The "input atom" (1, 2) of each spin lead and the final "output atom" form a magnetically frustrated triple with an anti-ferromagnetic coupling which constitutes the logic gate. The field pulse $\boldsymbol{B}_{\text{pulse}}$ is used to switch the inputs. The magnetic tip of an STM is used to construct and characterize the device. **b–e** Side view 3D topographs colored with the simultaneously measured SPSTS image of the constructed OR gate for all four possible input permutations (bright and dark contrasts correspond to states (1) and (0), respectively). By applying out-of-plane magnetic field pulses of different strength and direction, each input island can be controllably switched and the two spin leads transmit the information to their end atoms. The output atom in the gate triple reflects the logical operation of the inputs according to the indicated numbers reflecting the truth table [17]

atoms 1 and 2) and an additional output atom, which together form an equilateral antiferromagnetic triple with a smaller RKKY interaction as inside the chains. Using this equilateral configuration, the output atom will align antiparallel to the two input atoms if these are in the same magnetization state. However, if the two input atoms are in a different magnetization state, the output atom will be in a frustrated state, i.e. the two orientations perpendicular to the surface are degenerate. By using a small bias magnetic field, one of the two orientations will be preferred, which finally determines the logical operation of the gate as a function of the states of the two inputs.

The experimental realization of such a logic gate is shown in Fig. 1.12b. Two chains of 5 Fe atoms with an interatomic distance of $d = 0.923$ nm have been assembled on Cu(111) resulting in strong antiferromagnetic coupling (Fig. 1.10). The chains were assembled in such a way that the atoms on one of the ends of each chain were positioned close to the corner of a ferromagnetic Co island, while the two atoms on the other end of each chain have a mutual distance of $d = 1.35$ nm. Thereby, both chain ends are strongly antiferromagnetically coupled to the islands, but the mutual interaction between the two chains is kept smaller as the interaction within each chain. Finally, the output atom is positioned at the same distance of $d = 1.35$ nm to both chain ends.

The operation of the gate is shown in the spin-resolved images in Fig. 1.12b–e. By using magnetic field pulses of appropriate strength, the two Co islands, which have different size and therefore different coercivity, were put into the four different states (11), (10), (01), (00) as revealed by the spin-resolved images. Obviously, the magnetization states of both chains are following the states of their respective input island thereby transmitting the input to the gate region. Here, the output atom is forced into the state (0) if and only if the inputs are in the state (00), which proves the operation of the gate as an OR gate.

An interesting question concerning the down scaling of such logic elements is how small the input islands can be made and still remain stable in either of their magnetization states. This relates to the very fundamental question of how many atoms such an island has to contain in order to behave like a permanent magnet showing remanence [30]. In order to answer these questions, clusters of a small number of direct-exchange coupled Fe atoms have been assembled on Cu(111) and Pt(111), and were investigated by time-resolved SPSTS of the telegraph signal of such clusters.

On the substrate Cu(111), a cluster of five Fe atoms constitutes a stable magnet [31]. An even smaller permanent Fe magnet can be made on the substrate Pt(111) as illustrated in Fig. 1.13 [18]. It consists of only three Fe atoms that have been assembled onto neighboring fcc lattice sites using STM-tip induced atom manipulation (Fig. 1.13e). Figure 1.13a–d show spin-resolved STM images of two of such Fe_3 clusters assembled with a separation of only 2.5 nm. In these images a larger or smaller apparent height of the cluster indicates its spin state up (1) or down (0), respectively. By feeding spin-polarized electrons with sufficient energy from the magnetic STM tip through one of the clusters, which was done between the acquisition of the images, it was possible to write its spin state. Thereby, all four possible spin states (01), (11), (10), and (00) of the two-Fe_3 cluster memory were prepared.

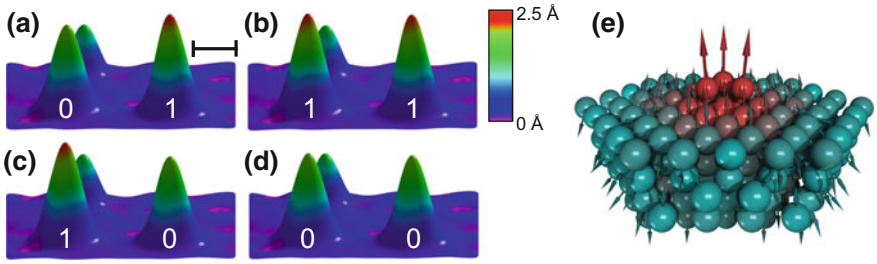

Fig. 1.13 **a–d** Spin-resolved STM images of the four possible spin states (01), (11), (10), and (00) of two Fe_3 clusters (0 and 1 correspond to downwards and upwards pointing magnetization, respectively). An additional Fe atom in the back serves as a marker for the apparent height. The scale bar has a length of 1 nm. **e** ab initio (KKR) calculation of the magnetic moments (arrows) in the Fe_3 cluster and the induced magnetization (color) in the substrate indicating their strong non-collinearity [18]

At the measurement temperature of 0.3 K these spin states were stable for at least 10 h.

The system of Fe_3 on Pt(111) is additionally interesting, as the heavy element Pt supports strong spin-orbit coupling and thereby a considerable DM contribution to the RKKY interaction (see Sect. 1.3.3). Consequently, the induced magnetization in the Pt underneath the cluster is highly non-collinear, as proven by ab initio calculations (Fig. 1.13e). Due to the resulting non-collinear RKKY interaction to neighboring magnetic atoms, the use of such a material combination in spintronic elements as the one shown in Fig. 1.12 might have advantages with respect to other materials, that feature only collinear states.

1.6 Conclusions

As we have shown in this review, the combination of SP(I)STS with STM-tip induced atom manipulation is a powerful experimental methodology to study the magnetic properties of artificial atomic-scale nanostructures. In particular, the magnetic moments, anisotropies, and g-factors of different atom/substrate systems, and the RKKY interaction in pairs have been measured directly. It was shown that the RKKY interaction offers a huge flexibility for tailoring the magnetic couplings in assembled nanostructures, ranging from ferromagnetic, over antiferromagnetic to non-collinear interactions. Due to this ultimate control of the atomic composition, positions and magnetic couplings, the results can be directly compared to model and ab initio calculations, in principle without the need to guess any unknown parameters. Finally, the knowledge was applied to build model systems for future atomic spintronic and information storage elements and we have shown that for all-metallic systems, a stable magnet requires only three Fe atoms on a Pt substrate.

Acknowledgements We thank the Deutsche Forschungsgemeinschaft DFG for the financial support of the project. AAK also acknowledges the DFG via the Emmy Noether Program (KH324/1-1). We gratefully acknowledge our colleagues Kirsten von Bergmann, Bruno Chilian, Jan Hermenau, Stefan Krause, Focko Meier, Tobias Schlenk, Andreas Sonntag, Manuel Steinbrecher, Khai Ton That, and Lihui Zhou, who were directly involved in the project. Furthermore, we thank Benjamin Baxevanis, Stefan Blügel, Mohammed Bouhassoune, Antonio T. Costa, Peter H. Dederichs, Manuel dos Santos Dias, Paolo Ferriani, Swantje Heers, Stefan Heinze, Christoph Hübner, Julen Ibañez-Azpiroz, Jindrich Kolorenc, Frank Lechermann, Alexander I. Lichtenstein, Samir Lounis, Phivos Mavropoulos, Doug L. Mills, Daniela Pfannkuche, Benjamin Schweflinghaus, Sergej Schuwalow, Alexander B. Shick, Markus Ternes, Maria Valentyuk, Elena Vedmedenko, and Tim O. Wehling for their theoretical support.

References

1. D.M. Eigler, E.K. Schweizer, Nature **344**(6266), 524 (1990)
2. A.J. Heinrich, J.A. Gupta, C.P. Lutz, D.M. Eigler, Science **306**(5695), 466 (2004)
3. F. Meier, L. Zhou, J. Wiebe, R. Wiesendanger, Science **320**(5872), 82 (2008)
4. A.A. Khajetoorians, T. Schlenk, B. Schweflinghaus, M. dos Santos Dias, M. Steinbrecher, M. Bouhassoune, S. Lounis, J. Wiebe, R. Wiesendanger, Phys. Rev. Lett. **111**, 157204 (2013)
5. A.A. Khajetoorians, S. Lounis, B. Chilian, A.T. Costa, L. Zhou, D.L. Mills, J. Wiebe, R. Wiesendanger, Phys. Rev. Lett. **106**, 037205 (2011)
6. B. Chilian, A.A. Khajetoorians, S. Lounis, A.T. Costa, D.L. Mills, J. Wiebe, R. Wiesendanger, Phys. Rev. B **84**, 212401 (2011)
7. C.F. Hirjibehedin, C.Y. Lin, A.F. Otte, M. Ternes, C.P. Lutz, B.A. Jones, A.J. Heinrich, Science **317**(5842), 1199 (2007)
8. T. Balashov, T. Schuh, A.F. Takács, A. Ernst, S. Ostanin, J. Henk, I. Mertig, P. Bruno, T. Miyamachi, S. Suga, W. Wulfhekel, Phys. Rev. Lett. **102**, 257203 (2009)
9. A.A. Khajetoorians, B. Chilian, J. Wiebe, S. Schuwalow, F. Lechermann, R. Wiesendanger, Nature **467**, 1084 (2010)
10. P. Wahl, L. Diekhöner, M.A. Schneider, L. Vitali, G. Wittich, K. Kern, Phys. Rev. Lett. **93**, 176603 (2004)
11. L. Zhou, J. Wiebe, S. Lounis, E. Vedmedenko, F. Meier, S. Blügel, P.H. Dederichs, R. Wiesendanger, Nat. Phys. **6**(3), 187 (2010)
12. C.F. Hirjibehedin, C.P. Lutz, A.J. Heinrich, Science **312**(5776), 1021 (2006)
13. N. Néel, R. Berndt, J. Kröger, T.O. Wehling, A.I. Lichtenstein, M.I. Katsnelson, Phys. Rev. Lett. **107**, 106804 (2011)
14. A.A. Khajetoorians, J. Wiebe, B. Chilian, S. Lounis, S. Blügel, R. Wiesendanger, Nat. Phys. **8**(6), 497 (2012)
15. A. Spinelli, B. Bryant, F. Delgado, J. Fernndez-Rossier, A.F. Otte, Nat. Mater. **13**(8), 782 (2014)
16. R. Toskovic, R. van den Berg, A. Spinelli, I.S. Eliens, B. van den Toorn, B. Bryant, J.S. Caux, A.F. Otte, Nat. Phys. **12**(7), 656 (2016)
17. A.A. Khajetoorians, J. Wiebe, B. Chilian, R. Wiesendanger, Science **332**(6033), 1062 (2011)
18. J. Hermenau, J. Ibañez-Azpiroz, C. Hübner, A. Sonntag, B. Baxevanis, K.T. Ton, M. Steinbrecher, A.A. Khajetoorians, M. dos Santos Dias, S. Blügel, R. Wiesendanger, S. Lounis, J. Wiebe, Nat. Commun. **8**(1), 642 (2017)
19. S. Loth, S. Baumann, C.P. Lutz, D.M. Eigler, A.J. Heinrich, Science **335**(6065), 196 (2012)
20. F.D. Natterer, K. Yang, W. Paul, P. Willke, T. Choi, T. Greber, A.J. Heinrich, C.P. Lutz, Nature **543**(7644), 226 (2017)
21. P. Gambardella, S. Rusponi, M. Veronese, S.S. Dhesi, C. Grazioli, A. Dallmeyer, I. Cabria, R. Zeller, P.H. Dederichs, K. Kern, C. Carbone, H. Brune, Science **300**(5622), 1130 (2003)

22. F. Meier, K. von Bergmann, P. Ferriani, J. Wiebe, M. Bode, K. Hashimoto, S. Heinze, R. Wiesendanger, Phys. Rev. B **74**, 195411 (2006)
23. G. Pacchioni, L. Gragnaniello, F. Donati, M. Pivetta, G. Autés, O. Yazyev, S. Rusponi, H. Brune, Phys. Rev. B **91**, 235426 (2015)
24. A.A. Khajetoorians, M. Valentyuk, M. Steinbrecher, T. Schlenk, A. Shick, J. Kolorenc, A.I. Lichtenstein, T.O. Wehling, R. Wiesendanger, J. Wiebe, Nat. Nanotechnol. **10**(11), 958 (2015)
25. D. Smith, J. Magn. Magn. Mater. **1**(3), 214 (1976)
26. A. Fert, P.M. Levy, Phys. Rev. Lett. **44**, 1538 (1980)
27. A.A. Khajetoorians, M. Steinbrecher, M. Ternes, M. Bouhassoune, M. dos Santos Dias, S. Lounis, J. Wiebe, R. Wiesendanger, Nat. Commun. **7**, 10620 (2016)
28. O. Šipr, S. Bornemann, H. Ebert, J. Minár, J. Phys. Condens. Matter **26**(19), 196002 (2014)
29. J. Bouaziz, M. dos Santos Dias, A. Ziane, M. Benakki, S. Blügel, S. Lounis, New J. Phys. **19**(2), 023010 (2017)
30. F. Donati, S. Rusponi, S. Stepanow, C. Wäckerlin, A. Singha, L. Persichetti, R. Baltic, K. Diller, F. Patthey, E. Fernandes, J. Dreiser, Ž. Šljivančanin, K. Kummer, C. Nistor, P. Gambardella, H. Brune, Science **352**(6283), 318 (2016)
31. A.A. Khajetoorians, B. Baxevanis, C. Hübner, T. Schlenk, S. Krause, T.O. Wehling, S. Lounis, A. Lichtenstein, D. Pfannkuche, J. Wiebe, R. Wiesendanger, Science **339**(6115), 55 (2013)
32. J. Wiebe, L. Zhou, R. Wiesendanger, J. Phys. D: Appl. Phys. **44**(46), 464009 (2011)
33. L. Zhou, F. Meier, J. Wiebe, R. Wiesendanger, Phys.Rev. B **82**, 012409 (2010)